



## Structure–activity relationships of Pt/Al<sub>2</sub>O<sub>3</sub> catalysts for CO and NO oxidation at diesel exhaust conditions

Alexey Boubnov<sup>a,b,1</sup>, Søren Dahl<sup>c,\*</sup>, Erik Johnson<sup>b</sup>, Anna Puig Molina<sup>a</sup>, Søren Bredmose Simonsen<sup>a,c</sup>, Fernando Morales Cano<sup>a</sup>, Stig Helveg<sup>a</sup>, Lived J. Lemus-Yegres<sup>a</sup>, Jan-Dierk Grunwaldt<sup>d,e</sup>

<sup>a</sup> Haldor Topsøe A/S, Nymøllevej 55, DK-2800 Lyngby, Denmark

<sup>b</sup> Niels Bohr Institute, Nano Science Center, University of Copenhagen, Universitetsparken 5, DK-2100 Copenhagen Ø, Denmark

<sup>c</sup> Center for Individual Nanoparticle Functionality, Department of Physics, Technical University of Denmark, Fysikvej, Building 307, DK-2800 Lyngby, Denmark

<sup>d</sup> Institute for Catalysis Research and Technology, Karlsruhe Institute of Technology, Hermann-von-Helmholtz-Platz 1, D-76344 Eggenstein-Leopoldshafen, Germany

<sup>e</sup> Institute for Chemical Technology and Polymer Chemistry, KIT, Kaiserstr. 12, D-76131 Karlsruhe, Germany

### ARTICLE INFO

#### Article history:

Received 27 March 2012

Received in revised form 19 July 2012

Accepted 25 July 2012

Available online 31 July 2012

#### Keywords:

Platinum  
Alumina  
Particle size  
CO oxidation  
NO oxidation  
Lean burn  
Surface oxide  
TEM  
Chemisorption  
*In situ* XAFS

### ABSTRACT

Structure–performance relationships for Pt/Al<sub>2</sub>O<sub>3</sub> catalysts with mean Pt particle sizes of 1, 2, 3, 5 and 10 nm are investigated for the catalytic oxidation of CO and NO under lean-burning diesel exhaust conditions. The most active catalysts for CO oxidation exhibit Pt particles of 2–3 nm, having a large fraction of low-coordinated and reactive surface Pt atoms. Exploiting *in situ* XAFS, we find that a reversible Pt surface oxidation is connected to high CO conversion. NO oxidation is most efficient over the catalysts with the largest Pt particles mainly exhibiting surface Pt atoms on planar facets. An irreversible Pt oxide formation observed during NO oxidation is a possible deactivation route and we suggest that the most active sites for NO oxidation are the ones least prone to surface oxidation. When both CO and NO are present in the reaction mixture, activity is increased for both reactions, suggesting that CO oxidation actively regenerates the Pt surface for NO oxidation and vice versa. The effect is strongest for the NO oxidation activity.

© 2012 Elsevier B.V. All rights reserved.

## 1. Introduction

Diesel engines for light-duty vehicles are an attractive alternative to conventional gasoline engines because of their better fuel economy. On the other hand, more elaborate exhaust after-treatment systems are necessary to decrease toxic emissions from diesel vehicles. Emissions of hazardous pollutants are regulated by law, which demands that emissions are gradually further decreased over the next years [1]. For example, in the European Union new pollutant emission standards are planned with the Euro 6 standard in 2014 [2]. These regulations for emissions together with requirements for CO<sub>2</sub>-reduction call for improvement of internal combustion engines as well as exhaust after-treatment systems.

A diesel oxidation catalyst (DOC) installed in a train of catalysts for diesel exhaust after-treatment is responsible for catalysing the oxidation of carbon monoxide (CO) and uncombusted fuel to CO<sub>2</sub> and water, as well as the oxidation of nitric oxide (NO) to nitrogen dioxide (NO<sub>2</sub>) under lean-burn (oxygen-rich) conditions. NO<sub>2</sub> is removed at a later stage and plays an important role in soot oxidation and for promoting the fast selective catalytic reduction of NO<sub>x</sub> with ammonia [1,3]. Platinum is known to be an excellent oxidation catalyst [4] which typically consists of nanoparticles dispersed on a porous alumina support.

Platinum is scarce and therefore expensive, making it desirable to decrease its amount in the production of catalysts, while at the same time retaining the catalytic activity. One way of doing this is to increase the dispersion (the ratio of surface atoms to total atoms) of the noble metal by synthesising a catalyst with small Pt particles. Given that all surface sites are equally active, this is a sensible approach if the small particles are stable against sintering under operating conditions.

However, it has been demonstrated that the activity of catalysts based on supported fcc-lattice metallic particles smaller than about 4 nm strongly varies and this reflects the size-dependent

\* Corresponding author. Tel.: +45 45253192.

E-mail addresses: [soren.dahl@fysik.dtu.dk](mailto:soren.dahl@fysik.dtu.dk), [sordahl@fysik.dtu.dk](mailto:sordahl@fysik.dtu.dk) (S. Dahl).

<sup>1</sup> Present address: Institute for Catalysis Research and Technology, Karlsruhe Institute of Technology, Hermann-von-Helmholtz-Platz 1, D-76344 Eggenstein-Leopoldshafen, Germany.

variation of different low-coordinated surface atoms. Low-coordinated atoms are more reactive which in the *d*-band model is explained by an upward shift of the *d*-band [5,6]. Distribution statistics of the different types of surface atoms for different metallic particle sizes have been described in detail by van Hardeveld and Hartog [7]. Models of *fcc*-nanocrystallites has also been described by Lopez et al. [8] and Mavrikakis et al. for Au particles [9]; the latter was used by Gracia et al. for Pt particles [10], identifying three types of low-coordinated surface atoms, namely corner atoms, dominating the surface of Pt particles of about 1 nm, edge atoms most abundant on 2 nm particles and atoms of low-index crystal facets, constituting most of the surface area of larger particles. This relation between the size of the Pt particles and the coordination number of the Pt surface sites and the fact that the oxidation rates at the different surface sites under lean-burning conditions is not *a priori* known, makes it an open question, whether decreasing the Pt particle size alone can be used as a mean to optimise the catalytic performance in an economically favourable manner. A thorough study of the size-activity relationships is necessary to address this issue. In addition, this study should also be supported by investigations of the chemical state (i.e. oxidation state) of Pt under the highly oxidising reaction conditions to provide the structure of the working catalyst in order to properly account for the redox nature and activity of the different Pt surface sites.

Numerous investigations have been carried out to study the effect of Pt particle size on CO oxidation, some using reaction conditions close to stoichiometric [10–12], some using ultrahigh vacuum techniques to study the reaction on defined Pt facets [13] and some studying structure-dependent selectivity of CO oxidation in relation to fuel cell catalysis [14–16]. Additionally, modelling work was carried out since the 1970s starting with CO oxidation close to stoichiometric conditions to study and optimise the reaction conditions [17,18] and extending to diesel exhaust conditions [19]. However, there seems to still be a gap in the study of structure-activity relationships for CO oxidation over Pt catalysts under lean-burn conditions with relevance for diesel exhaust after-treatment.

Work exists that argues that CO oxidation is structure insensitive, where structure differences are defined to arise from either different single crystal orientations [20] or particle sizes [20,21]. These fundamental studies take care that the experiments are carried out at low pressures [20] and differential conditions [21], in order to avoid effects such as heat and mass transport limitations interfering with the data. In this work we obtain differential data, however, in order to explicitly reveal any effects that may let one catalyst be preferred instead of another our focus is also on more realistic conditions where close to full catalytic conversion can be achieved. Apart from gaining structure-activity relationships for NO oxidation over Pt catalysts at lean exhaust conditions [22,23], the main purpose here is to include NO is to investigate the influence of NO on the CO oxidation and vice versa. The reaction mechanisms for the two reactions are known to be different and structure-sensitivity is reported for both reactions [24,25].

Hence, we report here on the effect of the Pt particle size on the activity of the Pt/Al<sub>2</sub>O<sub>3</sub> catalyst under lean-burn working conditions, focusing on the oxidation of CO and NO. Reaction mixtures containing CO, NO, oxygen and water vapour were used for simulating diesel exhaust. Catalysts with mean Pt particle diameters of approximately 1 nm and 2 nm as well as larger particles were prepared and compared in their catalytic activity to derive size-activity relationships. The Pt oxidation state was studied by *in situ* X-ray absorption spectroscopy to identify the active Pt species for the relevant reactions.

**Table 1**

Post-synthesis ageing conditions of the catalysts.

Sample	Atmosphere	Temperature (°C)	Time (h)
1	No ageing		
2	N <sub>2</sub>	600	1
3	N <sub>2</sub>	750	4
4	1% O <sub>2</sub> in N <sub>2</sub>	600	1
5	1:2 air/N <sub>2</sub> , H <sub>2</sub> O vapour	600	4

## 2. Experimental

### 2.1. Catalyst samples

The initial catalyst sample was prepared by impregnation of  $\gamma$ -alumina with a Pt precursor according to previously established procedures [12,25,26], followed by reduction. The Pt loading of the resulting catalyst was 4.8% by weight as determined by ICP analysis.

The initial catalyst batch was divided into 1 g portions, each of which underwent thermal ageing in a tube furnace under controlled conditions (temperature and atmosphere) in order to obtain different Pt particle size distributions. Table 1 gives an overview of the ageing conditions.

The particle size of the catalysts was studied by transmission electron microscopy (TEM) using a Philips CM200 FEG electron microscope. The microscope was operated at a primary electron energy of 200 keV and a point resolution of 1.9 Å in TEM mode. From the electron micrographs of each sample, the particle size distributions were evaluated based on at least 400 particles. The images were acquired at magnifications corresponding to a pixel resolution in the range from 0.5 Å/pixel, for the samples with smallest particles, to 5 Å/pixel, for the samples with the largest particles. For each particle, the size was obtained by outlining the projected particle area by an ellipse and recording its area  $A_i$ , using the ImageJ software [27]. Because the circularity of each ellipse was always close to 1, the average diameter  $d_i$  was calculated using the formula of the circle  $A_i = \pi d_i^2/4$ . The number-averaged particle sizes  $d_n$  and surface-averaged particle sizes  $d_s$  (the average particle size that can be compared to the one obtained from hydrogen chemisorption) for each distribution were calculated by

$$d_n = \frac{\sum_i n_i d_i}{\sum_i n_i} \quad \text{and} \quad d_s = \frac{\sum_i n_i d_i^3}{\sum_i n_i d_i^2}$$

respectively, where  $n_i$  is the number of particles of size  $d_i$ . The dispersion of Pt (ratio of surface atoms to the total number of atoms) was determined by hydrogen chemisorption using the double isotherm method at 40 °C. Prior to the first isotherm, the sample was reduced in a hydrogen flow for 2 h at 400 °C, followed by evacuation to <10<sup>−3</sup> mbar and cooling to 40 °C. After the first isotherm, the sample cell was evacuated and the second isotherm was performed. The dispersion was calculated from the amount of H<sub>2</sub> strongly adsorbed on Pt, assuming an H/Pt ratio of 1, and from knowing the metal loading of the catalysts, similar to other chemisorption studies of Pt-based catalysts [10,14,28]. For a direct comparison with the results obtained by TEM, the surface-averaged particle sizes  $d_s$  were calculated from the dispersion  $D$  by assuming that the supported particles were hemispherical in shape and by using atomic parameters for Pt used originally by Spenadel and Boudart [29]. Specifically, the  $d_s$  was calculated by the relation

$$d_s = \frac{1.02}{D},$$

where  $d_s$  is given in units of nanometres ( $D$  is a dimensionless number between 0 and 1).

**Table 2**

Experimental conditions for the activity measurements with samples 1–5. All gas mixtures were in balance He and the space velocity was 50,000 h<sup>-1</sup>.

Experiment step	Gas mixture	Temperature range	Heating ramp
1	1% H <sub>2</sub>	Room temp–100 °C	5 °C/min
2	1000 ppm CO, 10% O <sub>2</sub> , 5% H <sub>2</sub> O	35 °C–200 °C	5 °C/min
3	1000 ppm NO, 10% O <sub>2</sub> , 5% H <sub>2</sub> O	35 °C–500 °C	10 °C/min
4	1000 ppm CO, 1000 ppm NO, 10% O <sub>2</sub> , 5% H <sub>2</sub> O	35 °C–200 °C, 200 °C–500 °C	5 °C/min, 10 °C/min

## 2.2. Catalytic activity

For studying the catalytic performance, CO and NO conversion was measured as a function of the temperature using a quartz tube plug flow reactor at a constant flow and close to ambient pressure. The gas composition was analysed at the reactor exit by an intensity-calibrated quadrupole mass spectrometer (Pfeiffer Vacuum). The reactor was connected to the gas feeding system equipped with mass flow controllers and located in a computer-controlled oven. The temperature was measured by a thermocouple located inside the reactor close to the catalyst bed on the downstream side.

Importantly to compare the samples directly in terms of their intrinsic activity normalised to the Pt surface area without having to model and extrapolate data, the amount of each sample was loaded such that the Pt surface area determined by hydrogen chemisorption (cf. Section 3.1) was equal in all catalyst beds. To achieve this, 50 mg of sample 5 was used and the weight of samples 1–4 was scaled (down) based on their (higher) dispersion in order to obtain an equivalent Pt surface area in all five catalyst beds (weights are given later in Section 3). The sample powders were pressed into pellets, crushed and sieved in the fraction 150–300 µm. The samples were mixed with granulated SiC to obtain a bed volume of 0.18 ± 0.02 cm<sup>3</sup> for all experiments.

Pure gases and gas mixtures in balance He were taken from gas cylinders (Air Liquide, purity 5.0) and mixed in the gas feeding system with mass flow controllers to achieve the required gas composition. Approximately 5% water vapour was introduced into the gas mixture by bubbling a portion of the gas through a water flask kept constantly at 40 °C. All gas lines were traced to 200 °C to avoid water condensation. To ensure the same initial state of all samples, they were reduced at 100 °C under a flow of 1% H<sub>2</sub> in He, followed by cooling to 35 °C. At all stages of the experiment, the total gas flow was 150 mL/min, corresponding to a space velocity of 50,000 h<sup>-1</sup> for the diluted catalyst bed.

Following the reduction pretreatment, the Pt reactivity was examined in three steps: first CO oxidation was examined, followed by NO oxidation and finally the combined CO and NO oxidation was studied. Measurements of CO conversion were done between 35 °C and 200 °C while heating the reactor up at 5 °C/min. NO conversion was measured up to 500 °C at a heating ramp of 10 °C/min. The measurement scheme is summarised in Table 2.

## 2.3. In situ XAFS

XAFS measurements were carried out at the synchrotron radiation facilities MAX-lab (Lund, Sweden) at the beamline I811

and ANKA (Karlsruhe, Germany) at the XAS beamline, using a Si(111) double crystal monochromator in both cases. Both the step-scanning EXAFS mode and the quick-scanning EXAFS (QEXAFS) mode of the monochromator were exploited. XAFS spectra were acquired at the Pt L<sub>3</sub> edge (11,564 eV) in transmission geometry.

The *in situ* spectroscopic cell used in this work for structural characterisation of the catalyst was developed and initially used for *in situ* XAFS studies by Clausen and Topsøe [30]. It is a stainless steel continuous flow reactor with Kapton X-ray windows. The reactor was connected to the gas feeding system equipped with mass flow controllers and a quadrupole mass spectrometer (Pfeiffer Vacuum) for gas analysis at the exit. To provide heating, an alumina furnace (Kanthal) with Kapton windows was placed over the reactor. Pure gases and gas mixtures in balance He (Air Liquide, purity 4.0) were mixed in the gas feeding system to obtain the desired gas mixtures. Water vapour was generated by dosing water through an evaporator and was fed into the reactor together with the gas mixture. Table 3 summarises the experimental procedure. EXAFS measurements were carried out on samples 1, 2 and 3 during CO oxidation, and samples 1 and 3 also during NO oxidation. Sample powders in the sieve fraction 75–125 µm were used in the experiments. Approximately 65 mg of sample was loaded into the cell; note that this together with a gas flow of 20 mL/min gives a space velocity more than an order of magnitude lower than that of the catalytic activity measurements. Although the conditions achieved in this way were probably non-differential, they were considered suitable to probe the catalyst state spectroscopically during exposure to the specific gas mixtures and in the entire conversion interval relevant for technical applications. The uniform packing of the catalyst powder inside the *in situ* cell has moreover contributed to the homogeneity of the sample and thus spectrum quality (see the discussion on *in situ* XAS cells by Bare and Ressler [31] and Grunwaldt et al. [32]).

EXAFS spectra were acquired on the as-prepared samples, after reduction at 100 °C under a flow of 20% H<sub>2</sub> in balance He, at 200 °C (or 300 °C in the case of NO oxidation) in the reaction mixture consisting of 1000 ppm CO (or NO) and 10% O<sub>2</sub> in balance He and at room temperature in He after reaction. The samples were re-reduced with 20% H<sub>2</sub> in balance He at 100 °C and an EXAFS spectrum was acquired at room temperature. For comparison, EXAFS spectra of Pt foil and PtO<sub>2</sub> were measured as reference samples. The latter was mixed with polyethylene powder and pressed into a pellet for measurement.

For studying dynamic changes in the Pt oxidation state during the different reaction conditions, an *in situ* quartz capillary micro-reactor was used, originally developed by Clausen et al. [33] and

**Table 3**

Experimental conditions for the *in situ* EXAFS measurements. Gas mixtures were in balance He. The gas flow/catalyst weight ratio was lower than in activity measurements by a factor of 60 (sample 1), 30 (sample 2) and 20 (sample 3).

Experiment step	Gas mixture	Flow	Temperature	EXAFS spectra
1	–	–	Room temp.	As-prepared
2	20% H <sub>2</sub>	10 mL/min	100 °C at 5 °C/min in 20%	H <sub>2</sub> at room temp.
3	1000 ppm CO (or NO) 10% O <sub>2</sub> 5% H <sub>2</sub> O	20 mL/min	200 °C for CO (or 300 °C for NO)	In reaction mixture at maximum temp.
4	He	20 mL/min	Room temp.	In He at room temp.
5	20% H <sub>2</sub>	10 mL/min	100 °C at 5 °C/min	In 20% H <sub>2</sub> at room temp.



**Table 4**

Experimental conditions for *in situ* QEXAFS measurements. Heating and cooling took place between room temperature and the given temperature at the indicated ramp. Gas mixtures were in balance He. The gas flow/catalyst weight ratio was the same as for the activity measurements. The space velocity was not reproduced here as no dilution of the catalyst was applied.

Experiment step	Gas mixture	Flow	Temperature
1	5% H <sub>2</sub>	50 mL/min	100 °C at 5 °C/min
2	1000 ppm CO 10% O <sub>2</sub> 3% H <sub>2</sub> O	50 mL/min	160 °C at 3 °C/min
3	5% H <sub>2</sub>	50 mL/min	100 °C at 5 °C/min
4	1000 ppm NO 10% O <sub>2</sub> 3% H <sub>2</sub> O	50 mL/min	380 °C at 4 °C/min
5	1000 ppm CO 1000 ppm NO 10% O <sub>2</sub> 3% H <sub>2</sub> O	50 mL/min	160 °C at 3 °C/min

further developed by Grunwaldt et al. [32]. The feeding of reaction mixtures took place in a similar manner to that described above. Sample **2** in the sieve fraction 100–200  $\mu\text{m}$  was loaded into the capillary and fixed with quartz wool. QEXAFS spectra were acquired during heating up and cooling down in similar reaction mixtures as above containing either CO or NO and a mixture of both, all in balance He under a total flow of 50 mL/min. Prior to experiments with the first two reactions, the catalyst was reduced at 100 °C in 5% H<sub>2</sub> in balance He. The experimental procedure is summarised in Table 4. In this case, 4.7 mg was loaded so that the ratio of catalyst to the flow of gas is the same as that in the catalytic activity measurements. In this way, the conversions should be similar in the relevant temperature ranges. The space velocity is different, as no dilution of the catalyst was applied in the *in situ* measurement.

#### 2.4. XANES and EXAFS analysis

XANES spectra were analysed using the Athena extension of IFEFFIT software [34]. The spectra were energy-calibrated and normalised. The O/Pt ratio was calculated from linear combination analysis of the XANES spectra, using PtO<sub>2</sub> and Pt foil as standards. The analogous calculation was made for sample **2** during heating and cooling in the reaction mixtures.

EXAFS analysis was performed on spectra taken at room temperature. For EXAFS analysis, the spectra were energy-calibrated, normalised and background-subtracted. The  $k^2$ -weighted EXAFS functions were Fourier transformed on the  $k$ -range of 2.2–12.3  $\text{\AA}^{-1}$  and refined for the first Pt–O and Pt–Pt coordination shells ( $R=0.5$ – $2.0$   $\text{\AA}$  and  $1.6$ – $3.2$   $\text{\AA}$ , respectively). The Debye–Waller factor  $\sigma$  was fixed to 0.11  $\text{\AA}$  for both shells. This value of the Debye–Waller factor, along with the backscattering amplitude factors and phase shifts were calculated by refining the spectra of PtO<sub>2</sub> and Pt foil on the corresponding  $d$ -ranges. Fixing the Debye–Waller factor to a constant value has made it possible to compare all of the fit results directly. The statistical uncertainty of the free parameters was also decreased. While this can introduce an error in itself, we considered the results reliable for assessing the differences in the amount of oxide and metal for the samples under different reaction conditions.

### 3. Results

#### 3.1. Pt particle size distributions and dispersion

Fig. 1 shows TEM images of samples **1**–**5** and the corresponding particle size distributions. The mean Pt particle sizes for each sample are given in Table 5. The results show that the mean Pt

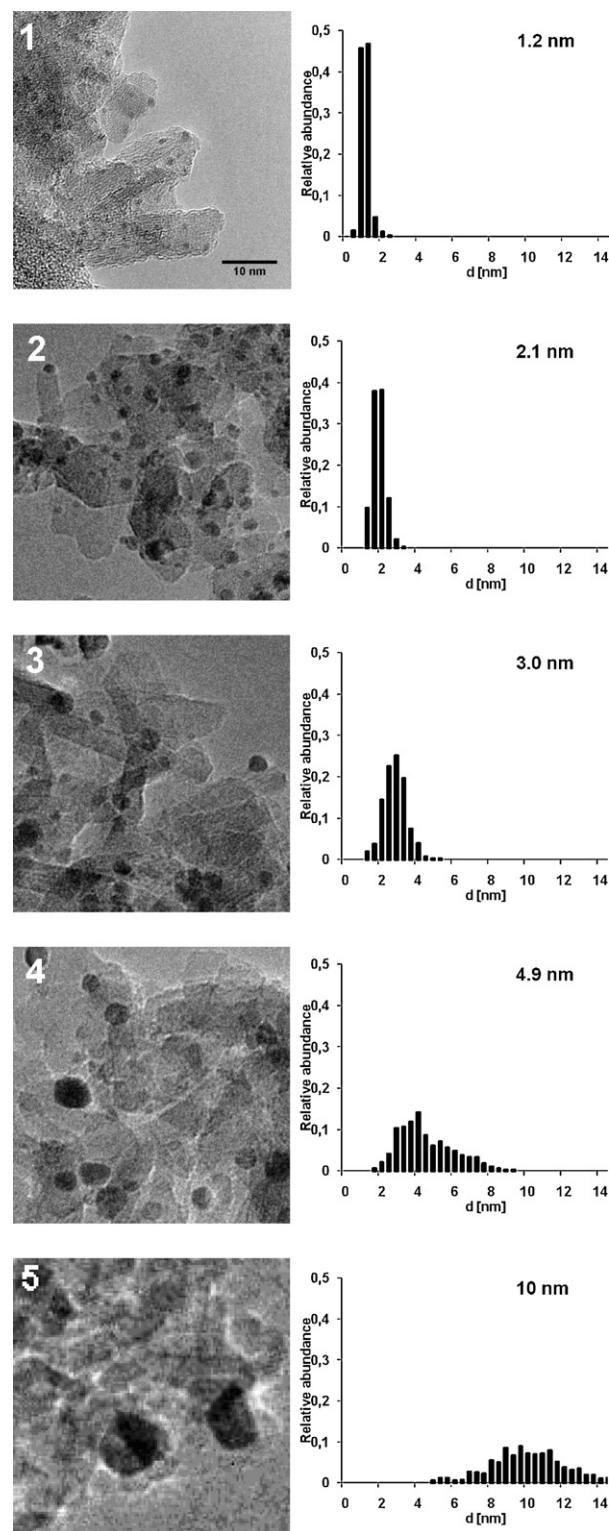


**Fig. 1.** TEM images of samples **1**–**5** and their corresponding Pt particle size distributions. The scale bar in the image of sample **1** is common for all images. Particle size abundance is normalised by the total number (>400) of measured particles. The mean particle size is given in each histogram.

particle size could be successfully controlled by choosing suitable thermal ageing conditions (Table 1) and the obtained samples can thus be used to study trends in the catalytic properties of the Pt/Al<sub>2</sub>O<sub>3</sub> system versus Pt particle size. However, thermal ageing will not only increase the particle size but also broaden the size distributions.

**Table 5**

Mean Pt particle sizes ( $d_n$ ) and surface-averaged Pt particle sizes ( $d_s$ ) obtained from particle size distributions and Pt dispersion ( $D$ ), surface-averaged Pt particle sizes ( $d_s$ ) and the amount of each sample used for the activity tests, calculated from  $H_2$  chemisorption (marked with \*).

Sample	$d_n$ [nm]	$d_s$ [nm]	* $D$	* $d_s$ [nm]	*Catalyst loading (mg)
1	1.2	1.3	0.76	1.3	8
2	2.1	2.2	0.43	2.4	14
3	3.0	3.2	0.24	4.3	25
4	4.9	5.6	0.23	4.4	26
5	10	11	0.12	8.5	50

Results from  $H_2$  chemisorption are shown in Table 5. To verify the chemisorption specificity of  $H_2$  on Pt, a control experiment was made with the alumina support alone and chemisorption was found to be negligible as compared to that on Pt-containing samples. The surface-averaged Pt particle sizes ( $d_s$ ) obtained from particle size distributions are generally consistent with those calculated from  $H_2$  chemisorption as shown in Table 5. Systematic differences are however noticed: chemisorption-determined  $d_s$  is slightly larger than particle size distribution-determined  $d_s$  in  $N_2$ -aged samples (2 and 3), while it is lower in samples aged in an oxidising atmosphere (4 and 5). These results may indicate that an oxidising atmosphere induces a certain amount of small Pt particles, which are undetectable in the present TEM inspections. A recent study has indeed shown that the sintering of Pt/ $Al_2O_3$  in an oxidising environment is fully dominated by Ostwald ripening, which is based on mobile atomic species and results in a tail of small particles [35].

### 3.2. Pt particle size effect on catalytic activity

Conversion profiles for CO and NO (reaction conditions, cf. Table 2) are presented in Fig. 2. Since these catalytic experiments were carried out with equal Pt surface area in the catalytic bed for all catalysts the conversions are directly related to the mean surface specific reaction rate or turn over frequency (TOF);  $TOF[s^{-1}] = Conv[\%]/1420$ . For conversion levels below 50% the TOF for CO oxidation is size-dependent and highest for Pt particles with a diameter of 2–3 nm; with smaller or larger particles lower TOF is attained. The TOF for NO oxidation is also size-sensitive; it increases steadily with increasing Pt particle size, indicating that large particles possess the most active NO oxidation sites. At higher temperatures, NO conversion is decreased as the reactant NO is favoured in the thermodynamic equilibrium with the product  $NO_2$  [28]. Only at differential conditions the conversion can be transformed into an intrinsic TOF since at higher temperature the conditions are very different in the inlet and outlet of the reactor and transport limitations will probably also be important. However, the ranking of the catalysts at high conversion is still valid and interesting from a technological point of view.

The corresponding results during oxidation of a mixture of CO and NO are shown in Fig. 3. The shape of CO conversion curves can be interpreted in terms of two high-activity regimes: low-temperature activity up to approximately 90 °C (indicated by arrows in Fig. 3A) superimposed onto the sigmoid conversion curve at higher temperatures similar to that in Fig. 2A. Note that prior to this measurement, the catalysts were tested for NO oxidation only and were not reduced in  $H_2$ , which probably affects the low-temperature reaction rate. Therefore in these experiments we focus on the high temperature high conversion behaviour where the

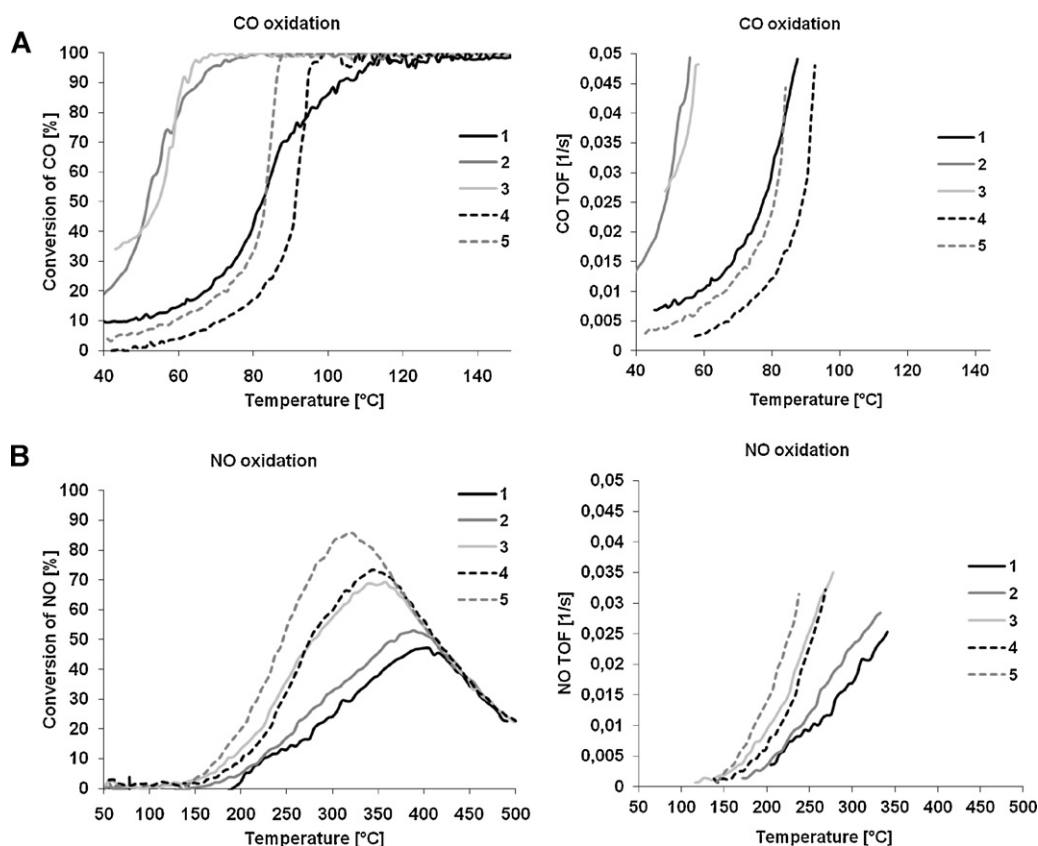


**Fig. 2.** (A) CO conversion over freshly reduced samples 1–5 exposed to 1000 ppm CO + 10%  $O_2$  + 5%  $H_2O$  and the corresponding CO TOF based on differential low conversion data (B) NO conversion and NO TOF over samples 1–5 exposed to 1000 ppm NO + 10%  $O_2$  + 5%  $H_2O$  (B). The catalyst loading was adjusted so that each bed contained the same Pt surface area. The gas mixtures were in balance He and the space velocity was 50,000  $h^{-1}$ .

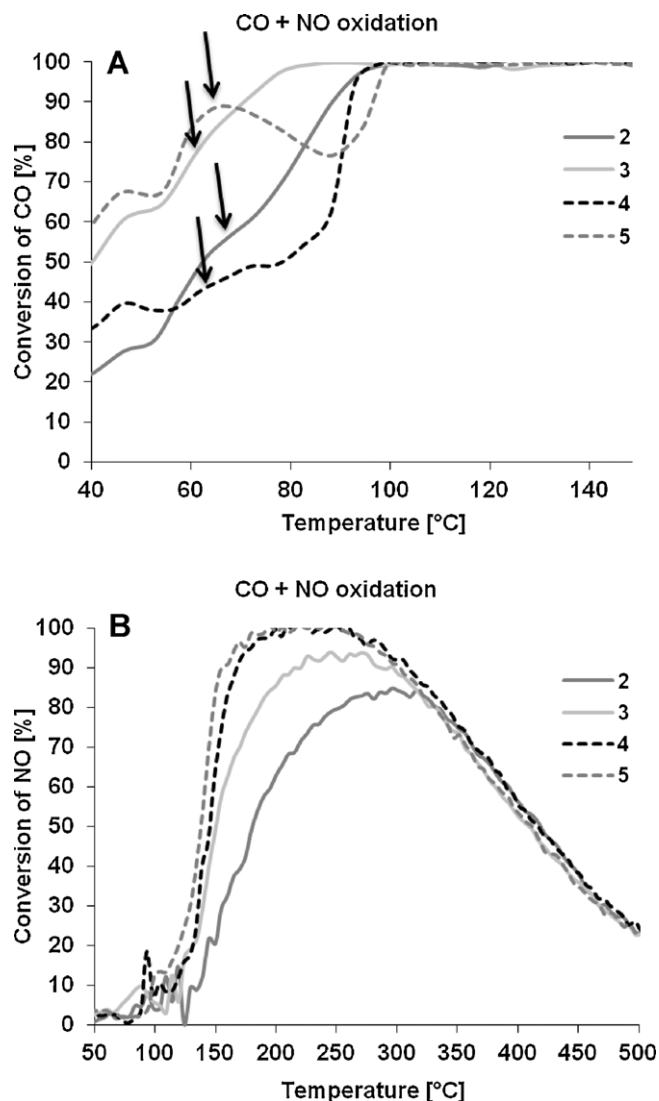


**Fig. 3.** CO conversion (A) and NO conversion (B) over samples 2–5 exposed to 1000 ppm CO + 1000 ppm NO + 10% O<sub>2</sub> + 5% H<sub>2</sub>O in balance He with a space velocity of 50000 h<sup>-1</sup>. Data for sample 1 are not shown as this sample showed a significant deactivation by sintering and was not considered suitable for drawing conclusions about the particle size–activity trends. The regimes of low-temperature CO oxidation activity in (A) are indicated by arrows.

prehistory of the catalyst does not play any important role. At these conditions there are in general only small differences between the CO only experiments and the NO plus CO experiments.

An exception was observed in the case of sample 1, which showed a large decrease of CO and NO conversion in the combined CO and NO experiment (not shown). This can be attributed to loss of Pt surface area due to sintering during the prior exposure to NO at elevated temperatures, since NO is known to induce sintering of Pt already at 200 °C [36]. It will be shown by EXAFS results later that sintering was observed for samples 1–3. The particle size almost doubled for sample 1 but the effect was only minor for samples 2 and 3. Therefore the trends in particle size–activity relationships are still valid for these two samples, while the results for sample 1 were not included in Fig. 3.

The trends for NO oxidation activity remain the same in the presence of CO as in its absence, but NO conversion increases significantly, the steep onsets of conversion taking place above ca. 120 °C, where CO is fully converted. Below this temperature, the NO conversion is low and its exact evaluation is difficult due to noise in

the data. Also, the NO conversion profiles over samples 4 (4.9 nm) and 5 (10 nm) are nearly coinciding, suggesting that this Pt particle size range has the highest TOF for NO oxidation in the presence of CO.

### 3.3. Pt oxidation state

XANES spectra of samples 1–3 exposed to different gases in the CO oxidation experiment are shown in Fig. 4. A key feature of these spectra is the white line (absorption maximum after the edge) corresponding to the 2p → 5d transition of the excited photoelectron in Pt, which is an important indication of the Pt oxidation state. The white line intensity was shown to be proportional to the atomic O/Pt ratio in Pt-based catalysts of known oxidation states [37]. We have adapted this relation and calculated the O/Pt ratio from linear combinations of PtO<sub>2</sub> (O/Pt = 2) and Pt foil (O/Pt = 0) as extremes; the results are presented in Table 6. The white line is lowest after the catalyst is reduced, while the as-prepared catalyst and that during and after exposure to the lean burn CO-containing gas mixture exhibit large white lines, indicating oxidised Pt. The overall differences between spectra of reduced and oxidised catalysts are most remarkable for the smallest particles (sample 1), while these differences are less pronounced in the case of larger particles (samples 2 and 3).

An understanding of the atomic structure of the catalysts at the different reaction conditions is facilitated by the EXAFS data analysis shown in Table 6. The coordination numbers and bond distances of the nearest O and Pt atoms should be compared to those in bulk Pt metal (CN<sub>Pt–Pt</sub> = 12, d<sub>Pt–Pt</sub> = 2.73 Å) and bulk PtO<sub>2</sub> (CN<sub>Pt–O</sub> = 6, d<sub>Pt–O</sub> = 2.09 Å). In the as-prepared sample 1, no Pt–Pt first-neighbour distances characteristic for metallic Pt were found, unravelling that the particles are fully oxidised and the absence of longer Pt–Pt contributions (not shown) demonstrates that the Pt clusters are highly dispersed. The Pt–O coordination numbers for this sample were the highest obtained (3.1–3.2) and together with the O/Pt ratios (0.54–0.74) this indicates that here, PtO<sub>x</sub> clusters with an under-stoichiometry of O (as compared to PtO<sub>2</sub>) are stabilised on the alumina surface. In the as-prepared samples 2 and 3, both Pt–O and Pt–Pt coordination shells were identified. The coordination numbers of the respective shells are complementary: a higher Pt–Pt coordination number means a lower Pt–O coordination number, consistent with a core–shell structure.

After the first reduction, only Pt–Pt contributions characteristic for metallic Pt were found, which is consistent with a full reduction of the Pt particles. The correlation between average Pt particle sizes (obtained by TEM and hydrogen chemisorption) and the nearest-neighbour Pt–Pt coordination number is closely comparable to correlations for small supported *fcc*-lattice metal particles found in literature [38,39].

After being exposed to the CO oxidation reaction mixture at 200 °C, sample 1 revealed the presence of both a Pt–O and a Pt–Pt coordination shell (Table 6, sample 1, CO oxidation), which can be interpreted as a metallic core–oxide shell structure. The remarkably low bond distance value of the Pt–Pt shell (2.67 Å) was atypical for distances in bulk Pt (2.73 Å), which is not surprising as the low Pt–Pt coordination number (2.4) corresponds to a metallic core of only a few Pt atoms, which can easily be susceptible to geometrical distortions. The high degree of oxidation of Pt is reflected by a Pt–O coordination number of 2.5 and an O/Pt ratio of 0.90. In fact, these characteristics of a small Pt core and decreased Pt–Pt bond distances are also seen for the as-prepared sample 2, but with higher Pt–Pt coordination numbers, lower Pt–O coordination numbers and a lower O/Pt ratio, demonstrating larger Pt particles.

Sample 2 after exposure to the CO reaction mixture showed Pt–Pt bond distances typical for bulk Pt metal and coordination numbers as high as 5.5 (in the presence of an oxide layer), while this

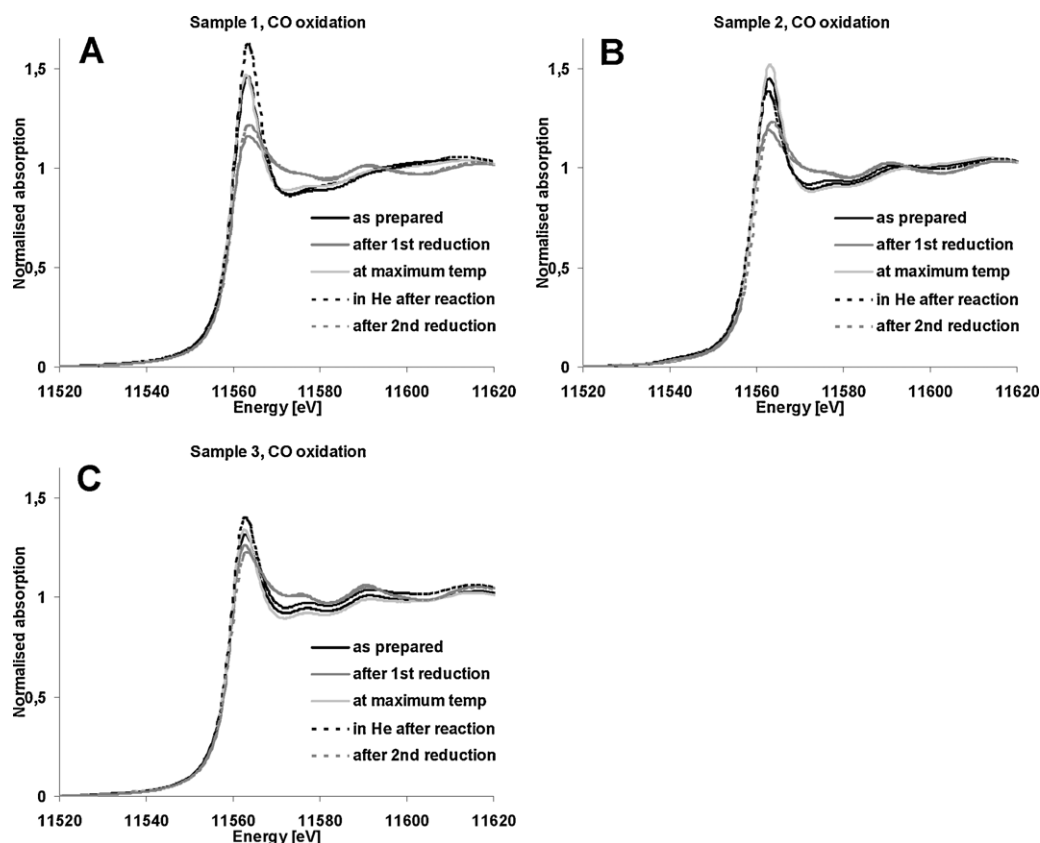


Fig. 4. XANES spectra of samples 1–3 during the five steps of the CO oxidation experiment (see Table 3).

coordination number is 8.5 after the first reduction (in the absence of an oxide layer). The Pt–O coordination number of 1.3 and the O/Pt ratio of 0.32 shows a lower extent of oxidation than sample 1; the bond distance of 2.19 Å seems rather untypical for an oxide; therefore we assign it to a high disorder of the structure and the small backscattering path. Such a value for a bond distance could possibly arise when using a single coordination shell to fit what is in reality two or more weak EXAFS contributions. Care must be taken to evaluate weak EXAFS scattering paths such as Pt–O, as the uncertainty might be greater than expected.

Sample 3 showed after exposure to the CO reaction mixture Pt–O and Pt–Pt bond distances characteristic for PtO<sub>2</sub> and Pt foil and

coordination numbers demonstrating well a core–shell structure of the Pt particles.

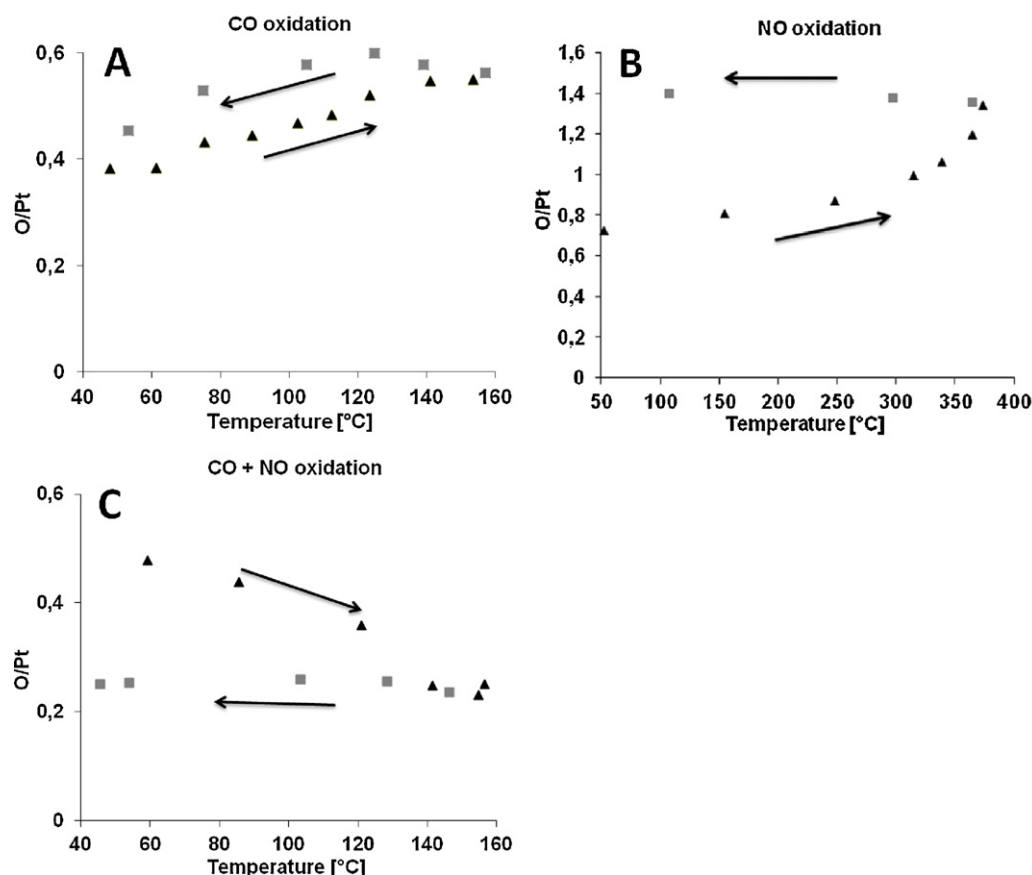
After NO oxidation, sample 1 exhibited rather high Pt–O and Pt–Pt coordination numbers (both higher than those of sample 2 after CO oxidation), showing that the Pt particles sintered and oxidised to a significant degree (O/Pt = 0.66) under the reaction mixture. The Pt–Pt bond distance is characteristic for metallic Pt. On the other hand, the Pt–O distance (2.01 Å) shows a strong deviation from that of PtO<sub>2</sub> (2.09 Å), which we again attribute to a disordered structure. Note that a TEM investigation (not shown) of sample 1 after the NO oxidation experiment has shown that most of the Pt particles sintered to a size of about 2 nm, but also a small amount

Table 6

Bond distances (*d*) and coordination numbers (CN) of the first coordination shells, calculated from EXAFS spectra. Backscattering paths analysed are Pt–O and Pt–Pt. The Debye–Waller factor  $\sigma$  was fixed to 0.11 Å in all cases. Standard errors for *d* are 0.02 Å and for CN are 0.5. O/Pt ratios calculated from linear combination analysis of the XANES spectra are given where oxidised Pt is present. <sup>a</sup>Note that a one-shell fit for Pt–O may not be sufficient for this analysis.

CO oxidation	Sample 1 (1.2 nm)				Sample 2 (2.1 nm)			Sample 3 (3.0 nm)		
	Bs. path	<i>d</i> [Å]	CN	O/Pt	<i>d</i> [Å]	CN	O/Pt	<i>d</i> [Å]	CN	O/Pt
As prepared	Pt–O	2.11	3.1	0.54	2.11	2.3	0.50	2.06	1.3	0.22
	Pt–Pt	–	–		2.67	3.4		2.70	7.6	
After 1st reduction	Pt–Pt	2.72	7.9		2.73	8.5		2.73	11.0	
After reaction in He	Pt–O	2.11	2.5	0.90	2.19 <sup>a</sup>	1.3	0.32	2.10	1.6	0.37
	Pt–Pt	2.67	2.4		2.73	5.5		2.72	7.5	
After 2nd reduction	Pt–Pt	2.73	9.1		2.73	9.1		2.74	11.6	
NO oxidation	Sample 1 (1.2 nm)				Sample 3 (3.0 nm)					
	Bs. path	<i>d</i> [Å]	CN	O/Pt	<i>d</i> [Å]	CN	O/Pt			
As prepared	Pt–O	2.11	3.2	0.74	2.08	1.2	0.38			
	Pt–Pt	–	–		2.70	7.2				
After 1st reduction	Pt–Pt	2.74	7.1		2.73	11.0				
After reaction in He	Pt–O	2.01 <sup>a</sup>	2.7	0.66	2.09	2.6	0.56			
	Pt–Pt	2.72	5.9		2.72	6.1				
After 2nd reduction	Pt–Pt	–	–		2.73	10.9				





**Fig. 5.** Evolution of the Pt oxidation state (in terms of the O/Pt ratio calculated from linear combination analysis) in sample **2** (2.1 nm) exposed to 1000 ppm CO + 10% O<sub>2</sub> + 3% H<sub>2</sub>O (A), 1000 ppm NO + 10% O<sub>2</sub> + 3% H<sub>2</sub>O (B) and 1000 ppm CO + 1000 ppm NO + 5% O<sub>2</sub> + 3% H<sub>2</sub>O (C), all in balance He under a total flow of 50 mL/min. Black triangles are data points during heating; grey squares are data points during cooling; arrows indicate the temperature ramp to guide the eye.

of particles up as large as 10 nm were formed, which is averaged in the EXAFS data.

After exposure to the NO reaction mixture sample **3** showed Pt–O and Pt–Pt bond distances characteristic for PtO<sub>2</sub> and Pt and coordination numbers indicating a core-shell structure of the Pt particles. In comparison to this sample after CO oxidation, the oxide contribution (coordination number) is higher and the metallic content is lower, consistent with a higher oxide formation (O/Pt = 0.56) in the NO oxidation experiment.

After the second reduction, the Pt–Pt coordination numbers generally tend to be larger than after the first reduction. For instance, in the CO oxidation experiment the Pt–Pt coordination number increased from 7.9 to 9.1 for sample **1**. This can be assigned to the sintering of Pt during the course of the experiments. After the experiment, this sample was investigated by TEM and the obtained particle size distribution (not shown) indeed revealed that the Pt particles sintered to an average size of 2 nm. These results indicate a loss of surface area due to sintering of sample **1** when the sample is re-used for measurements, such as in the combined CO and NO oxidation experiment shown in Fig. 3A.

Dynamic changes in Pt oxidation state of sample **2**, studied by temperature-dependent QEXAFS during oxidation of CO, NO and the mixture of the two are presented in Fig. 5. In these experiments, the conversion of CO and NO were similar to those obtained over sample **2** in the catalytic activity measurements, therefore a comparison of activity data (Fig. 2A and B, sample **2**) and the XANES data (Fig. 5A and B) is possible. The freshly reduced catalyst was steadily oxidised during heating up in the CO oxidation mixture, while during cooling down the catalyst was re-reduced. This is an important difference to the stationary XANES measurements, where the

catalyst was cooled down under a flow of He. The Pt is thus partially oxidised to a similar extent in the as-prepared state oxidised by air (O/Pt = 0.55 at 160 °C) when the catalyst is most active, but is reversibly reduced and CO-poisoned at lower temperatures, lowering the activity, as also previously shown by Singh et al. [40]. When exposing the freshly reduced catalyst to the NO oxidation mixture (Fig. 5B), Pt was heavily oxidised during heating and stayed in this state (O/Pt = 1.4) during cooling. The oxide formation was accelerated above ca. 300 °C, which is the equilibrium-governed regime between NO and NO<sub>2</sub> (see Fig. 2B), supporting previously reported evidence that the oxide formation takes place due to decomposition of NO<sub>2</sub> on the Pt surface [28].

Upon exposure of the catalyst to a mixture containing CO and NO (Fig. 5C), a similar response to the reaction atmosphere is observed as in the CO-only experiment. Starting from an oxidised catalyst directly following the NO oxidation experiment, Pt is being reduced during heating up to 140 °C. During cooling, Pt is left in a relatively reduced state (O/Pt = 0.25). The fraction of oxidised Pt after cooling down in the CO + NO reaction mixture (Fig. 5C) is lower than that after cooling down in the CO reaction mixture (Fig. 5A), which is possibly due to sintering of the Pt particles and thus loss of surface area.

## 4. Discussion

### 4.1. Pt particle-dependent surface oxide formation

In the following, we will discuss the characteristics of oxide formation on the Pt particles which we observed in our XAS



experiments. This will address the particle size effect and the reaction conditions. The general observation was that the smallest Pt particles tend to have a higher fraction of oxidised atoms than larger particles, which is consistent with an already mentioned metal-core-oxide-shell structure because the samples were reduced after synthesis, meaning that re-oxidation would proceed from the surface. However, a few peculiarities were encountered in some of the cases.

Whereas the smallest Pt particles (sample **1**) were fully oxidised in the as-prepared state, as no Pt–Pt coordination shell was identified (Table 6), the under-stoichiometry of oxygen atoms shows that the average oxidation state is below Pt(II), indicating that the alumina support possibly plays a role in limiting the oxidation state to Pt(II). XPS studies have confirmed this by showing that Pt on the surface of Pt/Al<sub>2</sub>O<sub>3</sub> catalysts after oxidative treatments is stabilised as Pt(II) [22], which is also valid for other catalyst supports [41].

An interesting observation was made in the case of the as-prepared samples **1–3**, in that the O/Pt ratios (Table 6) and the Pt dispersion *D* (effectively the H/Pt ratio, Table 5) are practically identical (O/Pt = 0.54, 0.74 and H/Pt = 0.76 for sample **1**, O/Pt = 0.50 and H/Pt = 0.43 for sample **2**, O/Pt = 0.22, 0.38 and H/Pt = 0.24 for sample **3**), showing that on average, every surface Pt atom is oxidised by one O atom when exposed to air at room temperature (storing conditions).

The unusual Pt–O bond lengths found in EXAFS spectra measured in He at room temperature after heating up in reaction mixtures for CO oxidation over sample **2** ( $d_{\text{Pt-O}} = 2.19 \text{ \AA}$ ) and NO oxidation over sample **1** ( $d_{\text{Pt-O}} = 2.01 \text{ \AA}$ ) may be traced back to two reasons. The deviation from the otherwise reported Pt–O distances of around  $2.09 \text{ \AA}$  can be introduced as an error in EXAFS analysis, but can also represent real distances: it is possible for Pt–O lengths to adsorbed O and OH groups to vary between  $1.8 \text{ \AA}$  and  $2.3 \text{ \AA}$  depending on the adsorption geometry and site [6].

The EXAFS results from the CO oxidation and NO oxidation experiments altogether show that smaller Pt particles form more surface oxide than larger ones. That the degree of oxidation depends on the particle size agrees well with results from previous studies [42,43]. The conditions established during the NO oxidation experiment at  $300^\circ\text{C}$  were significantly more oxidising than the conditions established during the CO oxidation experiment at  $200^\circ\text{C}$ , possibly due to platinum oxide formation on reaction with NO<sub>2</sub> in the former case, while in the latter case, CO, being a reducing agent, can partly counteract the oxidation of the catalyst. The oxidised Pt surface is thus considered a consequence of the oxygen-rich reaction conditions rather than the active phase.

Note that due to non-differential conditions during the EXAFS measurements in the stainless steel *in situ* reactor (large catalyst amount, low gas flow), there was a risk that at high conversions, the catalyst probed by the X-ray beam might see no reactants (CO or NO) if they are fully converted upstream of the catalyst bed. Despite the reaction conditions can be optimised by increasing the space velocity, the differences between the state of the catalyst induced under CO oxidation conditions and NO oxidation conditions mentioned above remain clear: the presence of NO and/or NO<sub>2</sub> at  $300^\circ\text{C}$  induces higher surface oxidation and particle sintering (as mentioned previously) than even the O<sub>2</sub>/CO<sub>2</sub>/H<sub>2</sub>O mixture.

#### 4.2. Structure–activity relationship for CO oxidation

As seen in Fig. 2 the TOF for CO oxidation is approximately  $0.03 \text{ s}^{-1}$  in the temperature range  $50\text{--}90^\circ\text{C}$  depending on the Pt particle size. For recycle experiments where the inlet CO/O<sub>2</sub> ratio was 1/10 and the CO concentration 1% a TOF of  $0.03 \text{ s}^{-1}$  was observed in the temperature range  $90\text{--}150^\circ\text{C}$  [10], which is in good agreement with the present results given the large difference in gas composition in the two experiments. The highest TOF for CO

oxidation is observed for catalysts with Pt particles of 2–3 nm in size. In this size range, low-coordinated edge atoms on the Pt particles are presumably the dominant surface species [10]. A main criterion for high CO oxidation activity is thus the presence of low-coordinated edge Pt atoms. As seen in Fig. 2 the same conclusion holds for the high conversion results.

This result is interesting since a different criterion for high CO oxidation activity has been reported close to stoichiometric reaction conditions [11,12,40]. These studies concluded that during CO-poisoning of the Pt surface at low temperatures, no space is left for oxygen to co-adsorb and react with the CO molecules, and that the catalyst only becomes active at a temperature where the CO molecules start desorbing. This behaviour is explained by the fact that CO is a more favoured adsorbant on Pt than O<sub>2</sub>, even when the CO/O<sub>2</sub> ratio is 1/5 [40] and 1/10 [10]. The reason for this is that CO molecules pack more densely on the Pt surface, although they have a lower binding energy than atomic oxygen [44]. Under the abovementioned CO/O<sub>2</sub> ratios, large Pt nanocrystals whose surface is dominated by planar facets, are the most active towards CO oxidation, as CO more easily desorbs from facet than step sites [10,12]. Another argument for why CO poisoning is higher on small than on large Pt particles is directly related to the size: the dipole–dipole repulsion between the adsorbed CO molecules is diminished by the curvature of small Pt particles, leading to an increased CO coverage on those [11].

In the present work the CO/O<sub>2</sub> ratio is 1/100, which is realistic for diesel exhaust gas [45,46], meaning that the fraction of oxygen is 10–100 times higher than in the abovementioned reports. Whereas the competition between CO and O<sub>2</sub> molecules for adsorption sites is always in favour of CO in these previous studies, an opposite situation in the present work is possible, as the CO molecules in the reaction mixtures are highly outnumbered. This is supported by the results of *in situ* XANES, showing that Pt is being readily oxidised at temperatures well below  $100^\circ\text{C}$ , showing that O<sub>2</sub> has access to the catalyst surface. In contrast Allian et al. [21] report that even at the conditions of our study, the Pt surface should be saturated with CO at  $85^\circ\text{C}$ . We cannot exclude the possibility that our results are affected by exotherms of CO oxidation, which is overcome by Allian et al. by a significantly higher volumetric dilution of the catalyst than in our case. However, the effect will be small since the adiabatic temperature increase for oxidising 1000 ppm CO to CO<sub>2</sub> is by maximum 13 K. Note further that water vapour was included in the reaction mixtures and it could have a distinct promotion effect for CO oxidation over 2–3 nm Pt particles. In fact, for larger Pt particles water molecules were reported to preferentially serve as an oxygen source for the reaction [47].

Density functional theory calculations have shown that, at high oxygen concentrations, the most energetically favourable adsorption site for oxygen is the threefold hollow site at the ridges of the Pt(110)–(1 × 2) surface [48]. The same site has been shown to be the most active for CO oxidation under lean conditions [49]. The similarity between these theoretical findings and our results is that the high under-coordination of the Pt surface atoms, being the ridges of under-coordinated Pt atoms on the single crystal surface or edges of Pt nanoparticles, provides very active catalytic centres for CO oxidation. Interestingly, the most under-coordinated corner atoms of which there are many on 1 nm particles (sample **1**) do not seem to be the most active sites for CO oxidation. An explanation could be that CO poisons them under the present reaction conditions.

Our results have shown that the presence of NO in the reaction mixture is favourable for CO oxidation: high CO oxidation activity at low temperatures (Fig. 3A) is attributed to the availability of a large number of active surface oxide species produced by the NO oxidation reaction (Fig. 5B). This is a transient phenomena since these surface oxide species are rapidly reduced by CO and as a result, the net Pt oxidation state decreases (Fig. 5C) until both the CO and NO

oxidation reactions run in parallel at high rates where the CO oxidation rate is similar to the situation without presence of NO while the NO oxidation rate is significantly higher in the presence of CO than without.

#### 4.3. Structure–activity relationship for NO oxidation

The TOF for NO oxidation obtained from conversion measurements is found to be  $0.01 \text{ s}^{-1}$  at  $180^\circ\text{C}$  for 10 nm Pt particles and at  $280^\circ\text{C}$  for 1.2 nm particles, as seen in Fig. 2. In [22] a similar TOF was observed at  $280^\circ\text{C}$  for 7 nm Pt particles. Given that the latter result is obtained for an inlet gas containing 300 ppm NO and 170 ppm  $\text{NO}_2$  the difference is understandable since the reaction orders was found to be  $-0.89$  for  $\text{NO}_2$  and  $1.12$  for NO [22]. These numerically high reaction orders also make it difficult to derive an intrinsic TOF from the present experiments. The TOF for NO oxidation increase with increasing particle sizes, which also holds for the high conversion activity. This finding is consistent with Pt atoms in planar surfaces being the more active sites and agrees with literature, where Pt catalysts are found to be poisoned by a full layer of adsorbed atomic oxygen or a surface oxide, which is formed when  $\text{NO}_2$  decomposes [28,50,51]. Since NO oxidation takes place at lean reaction conditions, the catalyst activity becomes significant at a temperature when  $\text{O}_2$  starts desorbing from its surface, as verified by  $\text{O}_2$ -TPD experiments [28,50,51]. The irreversible surface oxidation can be seen from the XANES results (Fig. 5B) and the rather high degree of oxidation is supported by EXAFS showing that the Pt–O coordination numbers in samples 1 and 3 after the NO oxidation reaction are 2.7 and 2.6, respectively (Table 5).

Olsson and Fridell [28] reported that oxygen poisoning is strongest on low-coordinated Pt atoms, which further suggests that the planar surface atoms are the most effective for oxidation of NO. Also, unlike the case of CO oxidation where CO-poisoning plays a role in the activity, we do not consider the role of NO adsorption on Pt here, as NO oxidation is assumed to proceed via the Eley–Rideal mechanism [23], which is further supported by evidence that NO is completely removed from Pt in the presence of  $\text{O}_2$  [51].

When both CO and NO were present in the reaction mixture, an important observation was made: the conversion of NO was significantly higher than in the absence of CO (Fig. 3B). As mentioned before, this can be explained by CO regeneration of the oxygen poisoned catalyst surface. CO is using the oxide for its own oxidation and leaving behind a highly active catalyst for NO oxidation. The same conclusion was derived by Irfan et al. [24], who have observed an increase in NO conversion over titania-supported Pt catalysts when CO was added to the feed gas and Henry et al. [52], who have seen beneficial effects of a reductant (hydrocarbons) for NO oxidation. This result could also be interpreted in a way that the exothermic character of CO oxidation (especially at high conversions, Fig. 3A and B) provides heat for NO oxidation. On the other hand, the adiabatic gas temperature increase when the 1000 ppm CO is oxidised is as mentioned earlier only  $\sim 13 \text{ K}$ , so this and the fact that the catalyst experiences reduction during the combined CO and NO oxidation (Fig. 5C) supports the idea of catalyst regeneration by CO. The other observation that a full conversion of CO is required for NO oxidation (onset at ca.  $120^\circ\text{C}$ , Fig. 3A and B) can be explained in that the product  $\text{NO}_2$  preferentially oxidises CO and goes back to NO at lower temperatures, inhibiting the oxidation of NO, as also reported by Katere et al. [53]. At higher temperatures, there is no observed inhibition as the CO is fully converted. The interpretation of these observations and the origin of the synergetic CO/NO effect will be studied in more detail in future. Firstly, the preferential CO oxidation by  $\text{NO}_2$  at temperatures below  $120^\circ\text{C}$  can explain the increased CO

conversion and inhibited NO conversion (Fig. 3), but is contradicted by the fact that even in the absence of CO, NO is not being converted (Fig. 2B) at these temperatures, i.e. no  $\text{NO}_2$  is being produced in the gas phase. One possible explanation for these observations is that an NO-related surface species promotes the CO oxidation reaction. Secondly, it is not completely clear why deactivation by surface oxidation does not take place in the CO/NO mixture at higher temperatures after CO is completely converted. A possibility is that the synergetic CO/NO-effect takes place close to the beginning of the catalyst bed where CO is still present, i.e. it is a local effect. The effect can also take place parallel to deactivation mechanisms, which are not pronounced in the present experiments.

A better understanding of the complementary behaviour of CO and NO oxidation can be achieved by studying the reactions under transient conditions. Derrouiche and Bianchi [54] have presented evidence that the oxidation of CO is inhibited for a period of time when NO molecules are co-adsorbed. As this intuitively contradicts our findings, the origins of this behaviour can be clarified by for instance, switching an NO flow on and off during a CO oxidation experiment (and vice versa) at temperatures where the change in conversion is significant. Spectroscopic studies such as XAFS are necessary to elucidate the structural changes in the catalyst during these experiments and FTIR can identify the chemical species dominating the catalyst surface.

Finally, note that sample 4 (4.9 nm) is as active for NO oxidation as sample 5 (10 nm) when CO is present in the gas. Hence in the presence of CO, the smaller particle size of Pt is optimal for doing NO oxidation when optimising the usage of Pt. Above  $300^\circ\text{C}$ , the performance of all catalysts is the same (Fig. 3), meaning that in this regime the catalyst with 2 nm Pt particles is ideal in terms of Pt usage. Under the present conditions, this catalyst can provide 1:1 NO/ $\text{NO}_2$  mixtures to a downstream SCR catalyst for efficient  $\text{NO}_x$  removal at ca.  $200^\circ\text{C}$  and  $400^\circ\text{C}$  (frequently established working temperatures in diesel oxidation catalysts on vehicles). Further studies will be necessary to extend these model powder catalysts to real technical monolithic catalysts.

## 5. Conclusion

In the study, Pt/ $\text{Al}_2\text{O}_3$  catalysts were designed with different distinct mean Pt particle sizes in the range 1–10 nm in order to obtain information about the size-dependent activity for the oxidation of CO and NO under oxygen-rich reaction conditions. CO oxidation was most efficient over Pt particles of 2–3 nm in diameter, consistent with the active sites being edges of the Pt crystals. In contrast, NO oxidation was more efficient over Pt particles larger than roughly 5 nm, suggesting that the reaction takes place on the planar crystal sites. Strikingly, NO conversion was significantly increased when CO was present in the reaction mixture, showing a synergetic effect of the two reactions. *In situ* XAS was found to be decisive to probe the state of the Pt particles under the different conditions. The measurements revealed that the Pt particles were surface-oxidised during both reactions, indicating that the Pt surface oxide formation plays an important role in the function of the catalysts under the present oxygen-rich reaction conditions. It was concluded that CO is most efficiently converted to  $\text{CO}_2$  over catalysts with low-coordinated Pt atoms which are most easily oxidised; the reaction is taking place between the CO molecule and an oxygen atom from the surface oxide. On the other hand, NO conversion is not optimal when the catalyst is oxidised; so-called oxygen poisoning of the catalyst inhibits NO oxidation. When both CO and NO are present in the reaction mixture, the CO ‘assists’ the NO conversion by removing the excessive oxide.

## Acknowledgements

The authors wish to thank MAX-lab (Lund, Sweden) and ANKA (Karlsruhe, Germany) for providing beamtime and S. Carlson (MAX-lab) and S. Mangold (ANKA) for support during the XAFS experiments. CINF is funded by the Danish National Research Council.

## References

- [1] M.V. Twigg, *Applied Catalysis B: Environmental* 70 (2007) 2–15.
- [2] Emission standards for diesel vehicles, <http://www.dieselnet.com/standards>.
- [3] E.S.J. Lox, B.H. Engler, F.J. Janssen, R.L. Garten, R.A. Dalla Betta, J.C. Schlatter, Z. Ainbinder, L.E. Manzer, M.J. Nappa, V.N. Parmon, K.I. Zamaraev, *Environmental Catalysis, Handbook of Heterogeneous Catalysis*, Wiley-VCH Verlag GmbH, 2008, pp. 1569–1595.
- [4] K.L. Fuldala, T.J. Truex, J.B. Nicholas, J.W. Woo, *Rational Design of Oxidation Catalysts for Diesel Emissions Control*, SAE International, 2008, 51–60.
- [5] B. Hammer, J.K. Nørskov, in: H.K. Bruce, C. Gates (Eds.), *Advances in Catalysis*, Academic Press, 2000, pp. 71–129.
- [6] B.C. Han, C.R. Miranda, G. Ceder, *Physical Review B* 77 (2008) 075410.
- [7] R. Van Hardeveld, F. Hartog, *Surface Science* 15 (1969) 189–230.
- [8] N. Lopez, J.K. Nørskov, T.V.W. Janssens, A. Carlsson, A. Puig-Molina, B.S. Clausen, J.D. Grunwaldt, *Journal of Catalysis* 225 (2004) 86–94.
- [9] M. Mavrikakis, P. Stoltze, J.K. Nørskov, *Catalysis Letters* 64 (2000) 101–106.
- [10] F.J. Gracia, L. Bollmann, E.E. Wolf, J.T. Miller, A.J. Kropf, *Journal of Catalysis* 220 (2003) 382–391.
- [11] G.S. Zafiris, R.J. Gorte, *Journal of Catalysis* 140 (1993) 418–423.
- [12] J. Yang, V. Tschamber, D. Habermacher, F. Garin, P. Gilot, *Applied Catalysis B: Environmental* 83 (2008) 229–239.
- [13] A. Szabó, M.A. Henderson, J.T. Yates, *Journal of Chemical Physics* 96 (1992) 6191–6202.
- [14] B. Atalik, D. Uner, *Journal of Catalysis* 241 (2006) 268–275.
- [15] F. Mariño, C. Descorme, D. Duprez, *Applied Catalysis B: Environmental* 54 (2004) 59–66.
- [16] D.H. Kim, M.S. Lim, *Applied Catalysis A: General* 224 (2002) 27–38.
- [17] R.E. Hayes, F.H. Bertrand, C. Audet, S.T. Kolaczowski, *The Canadian Journal of Chemical Engineering* 81 (2003) 1192–1199.
- [18] S.E. Voltz, C.R. Morgan, D. Liederman, S.M. Jacob, *Product R&D* 12 (1973) 294–301.
- [19] A. Pandya, J. Mmbaga, R. Hayes, W. Hauptmann, M. Votsmeier, *Topics in Catalysis* 52 (2009) 1929–1933.
- [20] M. Boudart, F. Rumpf, *Reaction Kinetics and Catalysis Letters* 35 (1987) 95–105.
- [21] A.D. Allian, K. Takanabe, K.L. Fuldala, X. Hao, T.J. Truex, J. Cai, C. Buda, M. Neurock, E. Iglesia, *Journal of the American Chemical Society* 133 (2011) 4498–4517.
- [22] S.S. Mulla, N. Chen, L. Cumaranatunge, G.E. Blau, D.Y. Zemlyanov, W.N. Delgass, W.S. Epling, F.H. Ribeiro, *Journal of Catalysis* 241 (2006) 389–399.
- [23] B.M. Weiss, E. Iglesia, *The Journal of Physical Chemistry C* 113 (2009) 13331–13340.
- [24] M.F. Irfan, J.H. Goo, S.D. Kim, S.C. Hong, *Chemosphere* 66 (2007) 54–59.
- [25] I.E. Beck, V.I. Bukhtiyarov, I.Y. Pakharukov, V.I. Zaikovskiy, V.V. Kriventsov, V.N. Parmon, *Journal of Catalysis* 268 (2009) 60–67.
- [26] H. Matsushashi, S. Nishiyama, H. Miura, K. Eguchi, K. Hasegawa, Y. Iizuka, A. Igarashi, N. Katada, J. Kobayashi, T. Kubota, T. Mori, K. Nakai, N. Okazaki, M. Sugioka, T. Umeki, Y. Yazawa, D. Lu, *Applied Catalysis A: General* 272 (2004) 329–338.
- [27] ImageJ software at National Institutes of Health, <http://rsbweb.nih.gov/ij/>.
- [28] L. Olsson, E. Fridell, *Journal of Catalysis* 210 (2002) 340–353.
- [29] L. Spenadel, M. Boudart, *The Journal of Physical Chemistry* 64 (1960) 204–207.
- [30] B.S. Clausen, H. Topsøe, *Catalysis Today* 9 (1991) 189–196.
- [31] S.R. Bare, T. Ressler, in: C.G. Bruce, K. Helmut (Eds.), *Advances in Catalysis*, Academic Press, 2009, pp. 339–465 (Chapter 6).
- [32] J.-D. Grunwaldt, M. Caravati, S. Hannemann, A. Baiker, *Physical Chemistry Chemical Physics* 6 (2004) 3037–3047.
- [33] B.S. Clausen, L. Gråbæk, G. Steffensen, P.L. Hansen, H. Topsøe, *Catalysis Letters* 20 (1993) 23–36.
- [34] M. Newville, *Journal of Synchrotron Radiation* 8 (2001) 322–324.
- [35] S.B. Simonsen, I. Chorkendorff, S. Dahl, M. Skoglundh, J. Sehested, S. Helveg, *Journal of the American Chemical Society* 132 (2010) 7968–7975.
- [36] P. Lööf, B. Stenbom, H. Norden, B. Kasemo, *Journal of Catalysis* 144 (1993) 60–76.
- [37] H. Yoshida, S. Nonoyama, Y. Yazawa, T. Hattori, *Physica Scripta* T115 (2005) 813–815.
- [38] I. Arcon, A. Tuel, A. Kodre, G. Martin, A. Barbier, *Journal of Synchrotron Radiation* 20 (2001) 575–577.
- [39] A. Puig-Molina, F.M. Cano, T.V.W. Janssens, *Journal of Physical Chemistry C* 114 (2010) 15410–15416.
- [40] J. Singh, E.M.C. Alayon, M. Tromp, O.V. Safonova, P. Glatzel, M. Nachttegaal, R. Frahm, J.A. van Bokhoven, *Angewandte Chemie-International Edition* 47 (2008) 9260–9264.
- [41] L.K. Ono, B. Yuan, H. Heinrich, B.R. Cuenya, *The Journal of Physical Chemistry C* 114 (2010) 22119–22133.
- [42] R.W. McCabe, C. Wong, H.S. Woo, *Journal of Catalysis* 114 (1988) 354–367.
- [43] C.-B. Wang, H.-K. Lin, S.-N. Hsu, T.-H. Huang, H.-C. Chiu, *Journal of Molecular Catalysis A: Chemical* 188 (2002) 201–208.
- [44] D.C. Ford, Y. Xu, M. Mavrikakis, *Surface Science* 587 (2005) 159–174.
- [45] H. Yamada, K. Misawa, D. Suzuki, K. Tanaka, J. Matsumoto, M. Fujii, K. Tanaka, *Proceedings of the Combustion Institute*, vol. 33, 2011, pp. 2895–2902.
- [46] H.H. Schenk, L.B. Berger, *American Journal of Public Health and the Nation's Health* 31 (1941) 669–681.
- [47] H. Muraki, S.-I. Matunaga, H. Shinjoh, M.S. Wainwright, D.L. Trimm, *Journal of Chemical Technology & Biotechnology* 52 (1991) 415–424.
- [48] S. Helveg, H.T. Lorensen, S. Horch, E. Lægsgaard, I. Stensgaard, K.W. Jacobsen, J.K. Nørskov, F. Besenbacher, *Surface Science* 430 (1999) L533–L539.
- [49] T.M. Pedersen, W.X. Li, B. Hammer, *Physical Chemistry Chemical Physics* 8 (2006) 1566–1574.
- [50] M. Crocoll, S. Kureti, W. Weisweiler, *Journal of Catalysis* 229 (2005) 480–489.
- [51] L. Olsson, B. Westerberg, H. Persson, E. Fridell, M. Skoglundh, B. Andersson, *Journal of Physical Chemistry B* 103 (1999) 10433–10439.
- [52] C. Henry, N. Currier, N. Ottinger, A. Yezerets, M. Castagnola, H.-Y. Chen, H. Hess, *SAE International* (2011) 371–383.
- [53] S.R. Katere, J.E. Patterson, P.M. Laing, *Industrial & Engineering Chemistry Research* 46 (2007) 2445–2454.
- [54] S. Derrouiche, D. Bianchi, *Journal of Catalysis* 242 (2006) 172–183.